Neuroinform
DOI 10.1007/s12021-014-9259-9

ORIGINAL ARTICLE

Impact of Early and Late Visual Deprivation on the Structure of the Corpus Callosum: A Study Combining Thickness Profile with Surface Tensor-Based Morphometry

Jie Shi · Olivier Collignon · Liang Xu · Gang Wang · Yue Kang · Franco Leporé · Yi Lao · Anand A. Joshi · Natasha Leporé · Yalin Wang

Abstract Blindness represents a unique model to study how visual experience may shape the development of brain organization. Exploring how the structure of the corpus callosum (CC) reorganizes ensuing visual deprivation is of particular interest due to its important functional implication in vision (e.g., via the splenium of the CC). Moreover, comparing early versus late visually deprived individuals has the potential to unravel the existence of a sensitive period for reshaping the CC structure. Here, we develop a novel framework to capture a complete set of shape differences in the CC between congenitally blind (CB), late blind (LB) and sighted control (SC) groups. The CCs were manually segmented from T1-weighted brain MRI and modeled by 3D tetrahedral meshes. We statistically compared the combination of local area and thickness at each point between subject groups. Differences in area are found using surface tensor-based morphometry; thickness is estimated by tracing the streamlines in the volumetric harmonic field. Group differences were assessed on this combined measure using Hotelling's T^2 test. Interestingly, we observed that the total callosal volume did not differ between the groups. However, our fine-grained analysis reveals significant differences mostly localized around the splenium areas between both blind groups and the sighted group (general effects of blindness) and, importantly, specific dissimilarities between the LB and CB groups, illustrating the existence of a sensitive period for reorganization. The new multivariate statistics also gave better effect sizes for detecting morphometric differences, relative to other statistics. They may boost statistical power for CC morphometric analyses.

Keywords Corpus Callosum Thickness · Volumetric Laplace-Beltrami Operator · Blindness · Multivariate Tensor-based Morphometry (mTBM)

Natasha Leporé and Yalin Wang are equal senior authors.

J. Shi · L. Xu · G. Wang · Y. Wang (✉)
School of Computing, Informatics, and Decision Systems Engineering, Arizona State University, P.O. Box 878809, Tempe, AZ 85287, USA
e-mail: ylwang@asu.edu

Y. Kang · Y. Lao · N. Leporé
Department of Radiology, Children's Hospital Los Angeles, Los Angeles, CA, USA

N. Leporé
Department of Radiology & Biomedical Engineering, University of Southern California, Los Angeles, CA, USA

O. Collignon
Center for Mind/Brain Science, University of Trento, Trento, Italy

G. Wang
School of Information and Electrical Engineering, Ludong University, Yantai, China

F. Leporé
Department of Psychology, University of Montreal, Montreal, QC, Canada

A. A. Joshi
Signal and Image Processing Institute, Brain and Creativity Institute, University of Southern California, Los Angeles, CA, USA

Introduction

Blindness is known to induce functional and structural brain reorganizations (Bavelier and Neville 2002; Noppeney 2007). In combination with recent advances in the collection and databasing of brain magnetic resonance imaging (MRI), anatomical and functional MRI analysis methods have begun to

Published online: 04 February 2015

shed light on blindness adaptation mechanisms (Amedi et al. 2003; Leporé et al. 2009; Jiang et al. 2009; Park et al. 2009; Bedny et al. 2011; Voss and Zatorre 2012; Wang et al. 2013a; Dormal et al. 2012; Collignon et al. 2011b). As a non-invasive and high-throughput analysis tool, neuroimaging can help better understand the neuroanatomical correlates of blindness, cross-modal plasticity and its relationship to sensitive/critical periods in brain development. The study of brain reorganization from blindness acquired at different developmental periods has therefore the potential to provide important new insights on how visual experience shapes the structure/function of specific brain regions (Ricciardi and Pietrini 2011; Collignon et al. 2009, 2013b). At a structural level, significant gray and white matter reductions throughout the visual system have been observed in early-blind individual (Noppeney et al. 2005; Pan et al. 2007; Ptito et al. 2008). Several groups have also shown significant atrophy in the geniculocortical tracts using diffusion imaging (Shimony et al. 2006; Park et al. 2007; Shu et al. 2009). The existence of important reorganizations of regions typically supporting the processing or the transfer of visual signals poses crucial challenges for sight-restoration (Merabet et al. 2005). Addressing this issue is particularly timely now given the recent advent of sight-restoration techniques including ophthalmologic procedures, stem cell transplantation, genetic therapies, as well as retinal prosthetic devices (Merabet et al. 2007; Veraart et al. 2004; Belluck 2013; Sieving et al. 2006). Beyond the remaining technical limitation of each procedure, the effects of rehabilitation therapies may depend on the integrity of the visual pathways and areas (Levin et al. 2010). Importantly, reorganization in brain structure typically supporting vision appears to depend on the period of blindness onset, with higher changes expected in association with early visual deprivation (Collignon et al. 2013a; Voss et al. 2013). A better understanding of how visual deprivation affects brain anatomy may therefore help rehabilitation prognostic and design in visually deprived individual candidates for sight restoration.

The corpus callosum (CC) is a particularly interesting subcortical structure to study in blind individuals (Leporé et al. 2010; Bock et al. 2013). The CC is the largest fiber bundle in the brain and establishes connections between the hemispheres, and predominantly, but not solely, between the cortical areas (Caleo et al. 2013). In particular, the splenium at the posterior end of the CC carries inter-hemispheric fibers connecting the visual areas of the brain. The splenium connects the right and left primary visual regions, which map the contralateral visual hemifields, in order to seamlessly integrate both visual fields across the vertical meridian (Pandya et al. 1971). Recently, a more detailed view of the structural organization of the splenium has been provided by demonstrating the existence of a dorsal/ventral mapping and eccentricity gradient of human splenial fibers (Dougherty et al. 2005). Moreover, the isthmus of the CC is involved in visuo-spatial processing, as it contains fibers connecting the posterior parietal areas of both hemispheres, which fuse multimodal sensory information (Hofer and Frahm 2006).

The CC undergoes extensive myelination during development until adolescence, and waves of peak growth rates can be observed in the CCs of children of different ages (Hua et al. 2009; Steele et al. 2013). Hence, studying the respective impact of congenital (CB) versus late blindness (LB) on the anatomy of the CC provides a unique model to probe how experience at different developmental periods shapes the structural organization of the brain (Noppeney 2007). However, how visual deprivation affects the structure of the corpus callosum is still a matter of debate. Some studies suggest that early acquired blindness leads to a reduction in splenial white matter volume (Leporé et al. 2010; Levin et al. 2010; Shimony et al. 2006). However, Bridge et al. (2009) did not find any structural differences within the splenium of anophthalmic subjects. Moreover, a recent study demonstrated that the large-scale topographic organization of visual callosal connections within the splenium (dorsal/ventral and eccentricity mapping) remains unaffected in early blind individuals (Bock et al. 2013). This last study therefore suggests that the gross retinotopic organization of visual fibers within the splenium develops and is maintained independently from any pre- or postnatal retinal input, and that changes as a result of blindness in this pathway may occur as white matter connections innervate cortex, rather than within the tracts themselves .

To ensure the use of all the shape information available in CC, we propose a novel analysis pipeline that includes the whole 3D CC structure (Xu et al. 2013b). We model the CC with 3D tetrahedral meshes and combine CC area and thickness measures in a vector at each vertex to be used as a metric for the statistical analysis of CC shape morphometry. To calculate thickness, we apply the volumetric Laplace-Beltrami operator proposed in our prior work (Wang et al. 2004a), which is now the de facto standard in volumetric harmonic map research (Wang et al. 2004b, 2012a, 2013b; Li et al. 2007, 2013; Tan et al. 2010; Pai et al. 2011; Paillé and Poulin 2012; Xu et al. 2013a). By solving the Laplace's equation, we construct a harmonic field on each of the CC tetrahedral meshes. Thickness is then determined from the streamlines of the harmonic field.

We use multivariate surface tensor-based morphometry to analyze differences in local area of the CC between subject groups. In the field of computational anatomy, tensor-based morphometry (TBM) (Davatzikos et al. 1996; Chung et al. 2008; Thompson et al. 2000) and more recently its multivariate extension, multivariate TBM (mTBM) (Leporé et al. 2008; Wang et al. 2010), have been used extensively to detect regional differences in surface and volume brain morphology between two groups of subjects (Wang et al. 2011, 2012c,

2013c; Shi et al. 2013a, c, 2014). Prior work (Wang et al. 2011; Shi et al. 2014) combining mTBM with other statistics such as the radial distance significantly improved statistical power. Intuitively, thickness and mTBM are complementary, as thickness describes distances roughly along the surface's normal direction, while mTBM detects surface dissimilarities, including differences in the surface metric tensor induced by the particular surface parameterization. So we hypothesize that the combination of thickness and mTBM will offer a complete set of surface statistics for callosal morphometry and that it may boost statistical power to detect the impacts of visual experience in the CC compared to 2D mid-sagittal analyses (Thompson et al. 2003; Luders et al. 2006, 2010; Tepest et al. 2010; Adamson et al. 2011; Di Paola et al. 2012; Herron et al. 2012).

In this paper, we combine thickness and mTBM to study callosal structural differences associated with congenital- versus late-onset blindness. Prior 2D TBM analyses of the corpus callosum (Leporé et al. 2010) revealed reductions in the isthmus and splenium of the corpus callosum in early but not late blind subjects when compared to sighted controls. Direct comparisons of the early and late blind groups did not find any significant changes, leaving open the question of how the period of visual deprivation impacts the structure of the CC. Here we set out to test whether subtle blindness related changes, especially between CB and LB, might be detected by our more powerful method.

Subjects and Methods

Subjects

Individuals with no history of neurological, cognitive or sensorimotor deficits other than blindness were included in the study and were divided into two groups. The first group consisted of 14 congenitally blind individuals (mean age± standard deviation (SD): 42.64±11.35; 10 males). The second group consisted of 11 late-onset blind subjects who lost vision after 8 years old (mean age±SD: 51.90±5.38; 3 males). Each of these groups was compared with a healthy group of 20 sighted controls (SC; mean age±SD: 38.30±13.48; 9 males). In all cases, blindness was attributable to bilateral peripheral damage (including: lenticular fibroplasia, retinoblastoma, tumors restricted to the eyes, retinal detachment, Leber's congenital amaurosis, retinas pigmentosa, accidents affecting the eyes and glaucoma) and led to total blindness. For brevity, we refer to congenitally and late-onset blind subjects as CB and LB for the rest of the paper.

The research protocol of the procedures was approved by the research ethic and scientific boards of the Centre for Interdisciplinary Research in Rehabilitation of Greater Montreal and the Quebec Bio-Imaging Network. Experiments were undertaken with the understanding and written consent of each subject.

Processing Pipeline Overview

Here we briefly overview the processing procedures to analyze CC morphometry. Following sections are detailed explanations of each step.

Figure 1 is the flow chart illustrating the overall sequence of steps in the processing pipeline. First, we manually segment the callosal volume from MRI scans, which is introduced in "Image Acquisition and Preprocessing" section. Second, based on the binary segmentation, we construct the tetrahedral mesh for each CC. The boundary of the tetrahedral mesh is a triangular mesh, which we call the CC surface. The construction of tetrahedral and triangular meshes is in "Tetrahedral Mesh and Triangular Mesh Generation" section. Third, we apply our in-house conformal mapping to introduce a regular conformal grid on each CC surface. Based on the conformal parameterization, each CC surface is decomposed into two parts: superior part and inferior part. The CC surface conformal parameterization and decomposition are detailed in "Surface Conformal Parameterization and Decomposition" section. Fourth, the thickness of a CC is computed by applying the volumetric Laplace-Beltrami operator to solve Laplace's equation on its tetrahedral mesh, where the superior and inferior parts of the CC surface are used as boundary conditions. Each point on the CC surface thus acquires a thickness measure. Detailed explanations of CC thickness computation are in "Callosal Thickness Computation" section. Fifth, we register the superior and inferior parts of the CC surface across subjects based on its conformal parameterization, where the thickness measures are interpolated on surface points. The CC surface registration is detailed in "Surface Registration" section. Finally, we compute the multivariate tensor-based morphometry (mTBM) statistics (Wang et al. 2010) and combine them with thickness measures to form a new multivariate statistic, which is applied to identify regions with significant differences between any two of the three groups. Permutation-based multiple comparison testes are used to estimate the overall significance (corrected p-values). The multivariate statistics and group difference analysis are introduced in "Multivariate Morphometry Features Computation" and "Statistical Maps and Analysis on Group Difference" sections, respectively.

Image Acquisition and Preprocessing

For each participant, a high-resolution volumetric MRI scan of the brain was acquired on a 3T MP-RAGE Siemens Tim Trio MRI Scanner (Siemens Electric, Erlangen, Germany). The scanning protocol was identical for all participants. A structural T1-weighted 3D MP-RAGE sequence scan (voxel

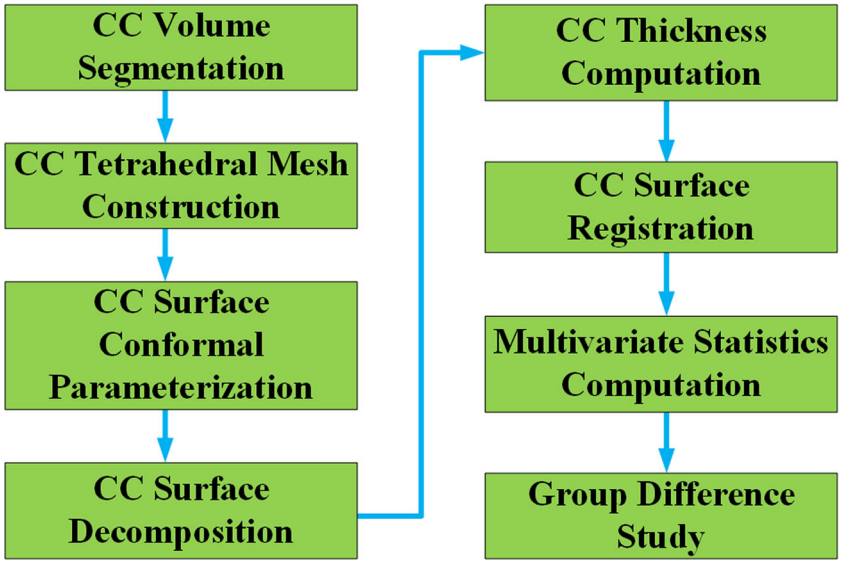

Fig. 1 Flow chart illustration of algorithm pipeline

size: $1\times1\times1.2mm^3$; matrix size: 256×240; slices: 160; sagittally-oriented MRI gradient echo sequence with repetition time (TR): 2300 ms; echo time (TE): 2.91 ms; inversion time (TI): 900 ms; and field of view (FoV): 256×240 mm^2) was acquired for each subject using the same scanner, equipped with a 12-channel head coil.

Images were aligned and scaled to the ICBM-53 brain template (International Consortium for Brain Mapping) with the FLIRT software (Jenkinson and Smith 2001), using nine-parameter linear transformations (three translations, three rotations and three scales). We manually segmented the CCs with Insight Toolkit's SNAP program (Yushkevich et al. 2006) as shown in Fig. 2. Tracings were performed by a trained investigator (Y.K.) and the results were checked by an experienced neuroscientist (F.L.). We consulted neuroanatomical references of the corpus callosum to help guide the placement of the contours. Our intra-rater average percent volume overlap (intersection of volumes over average of them) for four structures segmented twice at a few months interval is 90.07 %.

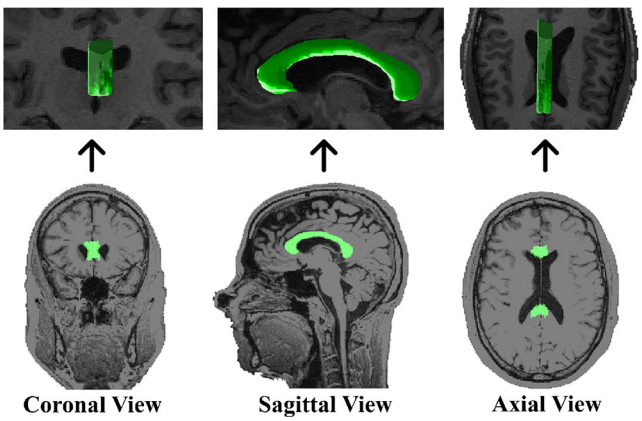

Fig. 2 Illustration of the corpus callosum (*CC*) segmentation results. On the *bottom row*, the segmented volumes are depicted in *green* and shown in three different views. The reconstructed callosal surface is overlaid on MR images on the *top row*

Multivariate Morphometric Analysis of the CC

Tetrahedral Mesh and Triangular Mesh Generation

Our tetrahedral meshes are generated by an adaptively sized tetrahedral mesh modeling method (Lederman et al. 2011). The method produces meshes conforming to the voxelized regions in the image by minimizing an energy function consisting of a smoothing term, a fidelity term and an elasticity term. Figure 3a shows an example of a tetrahedral mesh with a zoomed cut-plane view. The boundary of the tetrahedral mesh gives a triangular surface mesh for the callosal surface, which we call the CC surface (Fig. 3b).

Surface Conformal Parameterization and Decomposition

The goal of this step is to introduce regular conformal grids on CC surfaces and thus consistently decompose them into superior and inferior parts of surface patches for thickness computation.

Given the long and thin structure of a CC surface, existing area-preserving subcortical surface parameterization algorithms (e.g., (Styner et al. 2005a)) that map surfaces to spheres as a canonical space may produce large distortions. Instead, for accurate surface decomposition and registration, we adopt our holomorphic one-form based method (Wang et al. 2011) to compute a conformal parameterization for each CC surface.

First, given a callosal surface, we label two consistent landmark curves at the caudal and rostral endpoints. They are biologically valid and consistent landmarks across subjects

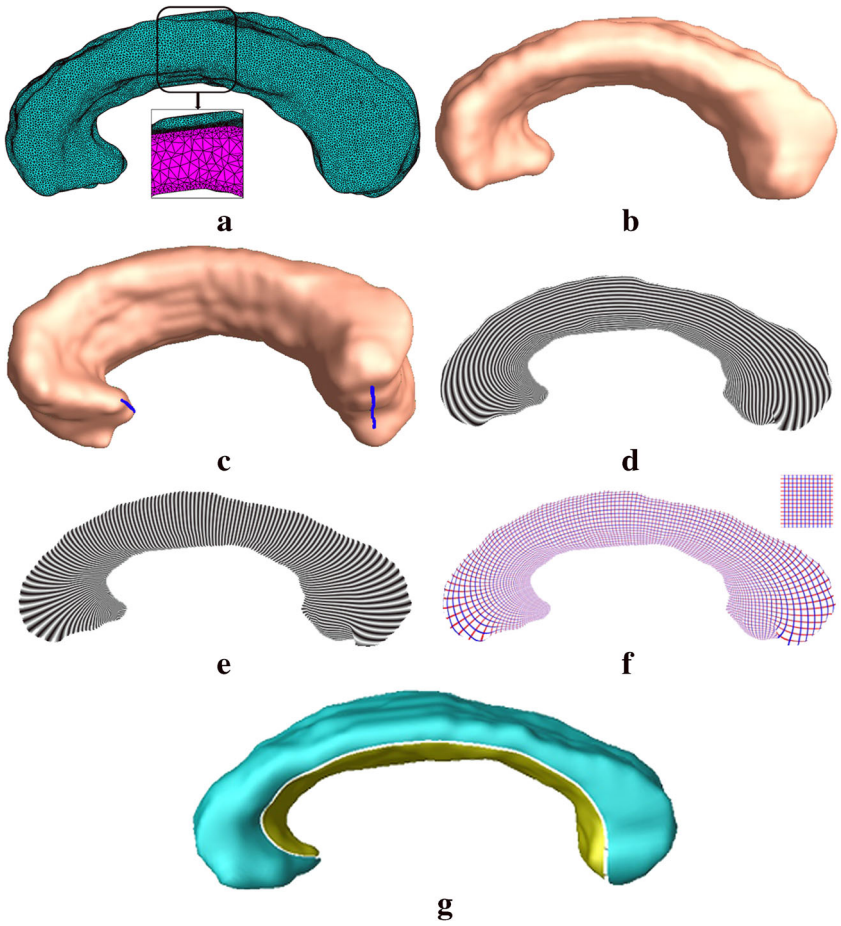

Fig. 3 Details of CC surface parameterization and decomposition. The CC tetrahedral mesh (**a**) is constructed based on the CC binary segmentation as shown in Fig. 2. The boundary of the tetrahedral mesh is a triangular mesh, which is called the CC surface (**b**). In order to compute its conformal parameterization, two biologically valid and consistent landmarks are introduced on each CC surface (**c**). By computing the exact harmonic one-form (**d**), the conjugate one-form (**e**), which is locally perpendicular to the one-form in (**d**), we finally obtain the canonical holomorphic one-form (**e**), which introduces a conformal parameterization for the CC surface. The conformality is visualized by texture mapping of a checkerboard image on the 3D CC surface. In **g**, the conformal parameterization is used to induce two iso-parametric curves, which cut the CC surface into two pieces, a superior one (*blue*) and an inferior one (*yellow*)

as shown in Fig. 3c (blue lines). After slicing each CC surface open along the two landmark curves, it becomes a genus-0 surface with two open boundaries. We call this process *topology optimization*. Given the callosal horizontal tube-like shape, these landmark curves can be automatically detected by checking the extreme points along the first principal direction of the geometric moments of the surface (Elad et al. 2004). We successfully applied similar techniques in a number of prior works (Wang et al. 2010, 2011; Monje et al. 2013; Colom et al. 2013; Shi et al. 2013a, c, 2014). This optimization provides biologically plausible landmarks which may improve the surface analysis on elongated or branching surfaces.

Next, we compute the exact one-forms (Fig. 3d) with the open boundary CC surfaces. Then we compute all closed but non-exact one-forms. The harmonic one-form basis is the union of the exact one-forms and the closed but non-exact one-forms. By solving a linear system with the harmonic one-form basis, we obtain the conjugates of the exact one-forms, which are locally perpendicular to the exact one-forms (Fig. 3e). The exact one-forms and their conjugate one-forms form the holomorphic one-form basis, which introduces a conformal grid on each CC surface (Fig. 3f). In Fig. 3f, the checkerboard texture is used to illustrate the angle-preserving property of the parameterization. For theoretical background and implementation details of holomorphic one-form based surface conformal parameterization, please refer to (Wang et al. 2011). The algorithm involves solving a few linear systems, thus it is quite stable and efficient.

On each of the parameterized CC surfaces, we generate two iso-parametric curves which pass the extreme points on two lateral sides. By cutting along these two curves and removing their attached triangles in the triangle mesh, we produce superior (Fig. 3g blue) and inferior (Fig. 3g yellow) surface patches, which are used for the callosal thickness computation and surface registration.

Callosal Thickness Computation

After the CC surfaces are decomposed into superior and inferior patches, we apply a tetrahedral mesh based algorithm to compute the callosal thickness. We adopt the volumetric Laplace-Beltrami operator developed in our prior work (Wang et al. 2004a), which is defined on the tetrahedral mesh, with the decomposed CC surfaces as boundary conditions. Compared with prior work on solving the Laplace's equation (e.g., (Jones et al. 2000; Adamson et al. 2011)), this approach may overcome numerical inaccuracies issues caused by the

limited resolution of the 3D grid in standard voxel-based thickness computations.

Given a tetrahedral mesh M, whose boundary is the CC surface ∂M, we denote the superior and inferior patches as ∂M^{+} and ∂M^{-}, respectively. We use v_i, v_j to denote vertices and $[v_i, v_j]$ to denote an edge connecting v_i, v_j. Let V be the set of all vertices on M, we define a piecewise linear function $f: V \rightarrow \mathbb{R}$. Suppose that every edge $[v_i, v_j]$ is assigned a string constant $k(v_i, v_j)$, then the *string energy* on the mesh is defined as the following quadratic form:

$$E(f) = < f, f > = \sum_{[v_i,\, v_j] \in K} k(v_i, v_j)\left(f(v_i) - f(v_j)\right)\left(f(v_i) - f(v_j)\right) \quad (1)$$

where K is the set of all edges in the mesh. As shown in Fig. 4a, in one tetrahedron, we say that edge $[v_1, v_4]$ is against edge $[v_2, v_3]$ and θ_{23} is the dihedral angle. Let l denote an edge length. Suppose an edge, $[v_i, v_j]$, which is shared by n tetrahedrons, is against n edges with lengths $l_r, r = 1, \ldots n$, and n dihedral angles, $\theta_r, r = 1, \ldots, n$, we can define the string constant as

$$k(v_i, v_j) = \frac{1}{12} \sum_{r=1}^{n} l_r \cot(\theta_r) \quad (2)$$

With this definition of $k(v_i, v_j)$, the string energy (Eq. 1) is called the *discrete harmonic energy* (Wang et al. 2004a). In our prior work (Xu 2013), we proved that the discrete harmonic energy is consistent with the traditional harmonic energy. Here the string coefficient $\frac{1}{12}$ is chosen to ensure that the quadratic form in Eq. 1 is positive definite (Gu et al. 2004).

The volumetric Laplace-Beltrami operator on a vertex v_i of the tetrahedral mesh is then defined as (Wang et al. 2004a):

$$\Delta_{LB} f(v_i) = \sum_{[v_i, v_j] \in K} k(v_i, v_j)\left(f(v_j) - f(v_i)\right) \quad (3)$$

If f minimizes the harmonic energy, then f satisfies the Laplace's equation $\Delta_{LB} f = 0$ and f is called a harmonic function. In this paper, in order to solve the Laplace's equation, we

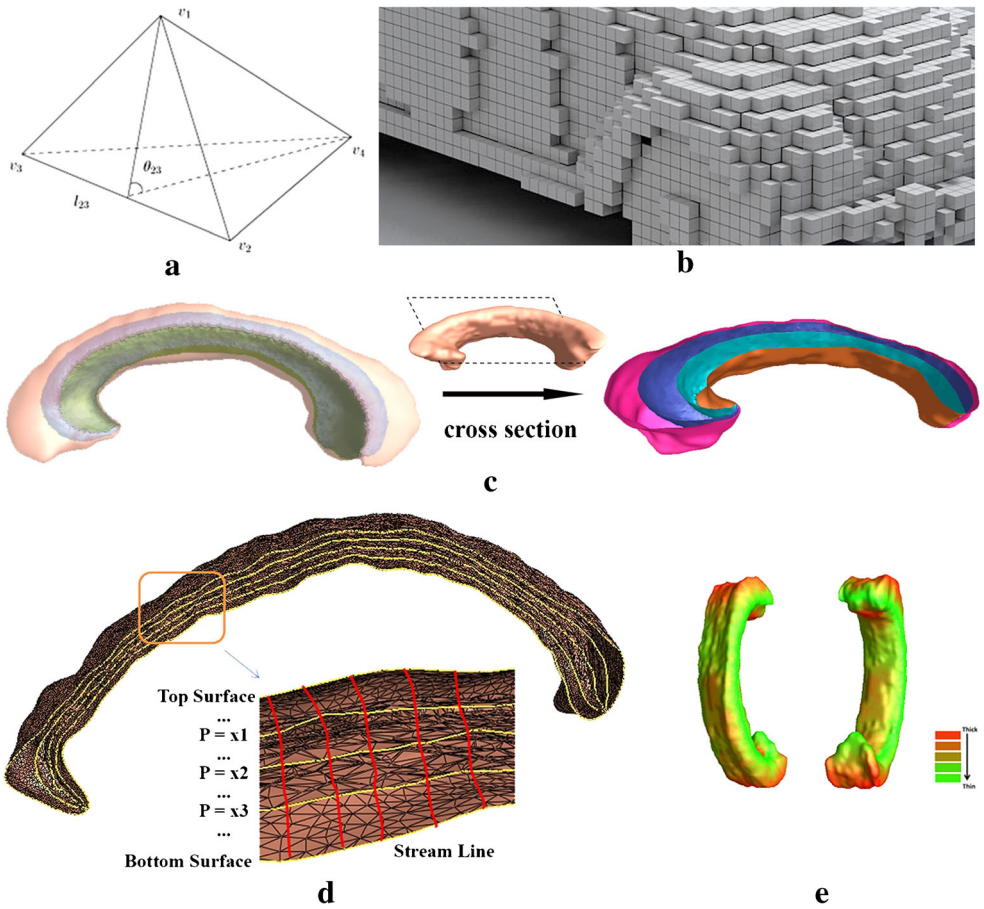

Fig. 4 Details of thickness computation on CC tetrahedral meshes. **a** Shows a tetrahedron example. We say that the edge $[v_1, v_4]$ is against $[v_2, v_3]$ and the dihedral angle, θ_{23}. This relationship is used to define the volumetric Laplace-Beltrami operator. **b** Shows a voxel mesh example (Wüstefeld 2010). In **c**, the equipotential level sets are shown as colored surfaces. The *left panel* is a global volumetric rendering with a transparent outer boundary. The *right panel* shows a zoomed-in picture of a cross-section along the sagittal direction. We then trace streamlines between the superior and inferior pieces of a CC surface along the normal directions of the level sets and the CC thickness is measured by the lengths of theses streamlines (**d**). **e** is the computed thickness color map illustrated on a callosal surface: the *red color* means thick and the *green color* means thin

use the volumetric Laplace-Beltrami operator to construct a linear system, whose solution is a function f that minimizes the harmonic energy.

In the implementation, we solve the Laplace's equation with the Dirichlet boundary condition. Specifically, we define the values of function f on vertices of the superior boundary ∂M^+ as 0 and those on vertices of the inferior boundary ∂M^- as 1. For all interior vertices on the tetrahedral mesh, their f values are unkown but satisfy $\Delta_{LB} f=0$. Thus, we define $f = \begin{cases} \Delta_{LB} f(v) = 0, & \forall v \notin \partial M \\ f(v) = 0, & \forall v \in \partial M^+ \\ f(v) = 1, & \forall v \in \partial M^- \end{cases}$ on the tetrahedral mesh M. Then we define following local stiffness matrix S for all interior vertices v_i on M:

$$S_{i,j} = \begin{cases} k(v_i, v_j), & [v_i, v_j] \in K \\ 0, & [v_i, v_j] \notin K \end{cases} \tag{4}$$

where $k(v_i,v_j)$ is defined in Eq. 2. Next, we add the contribution of the local stiffness matrix to the global stiffness matrix and define the discrete *volumetric Laplace-Beltrami operator* for a CC tetrahedral mesh as

$$L_p = D - S \tag{5}$$

where D, the degree matrix, is a diagonal matrix defined as $D_{i,i}=\sum_j S_{i,j}$.

Similar to surface spectral analysis (Chung 2012; Qiu et al. 2006a, b; Lombaert et al. 2013; Shi et al. 2010), we can construct a linear system to solve Laplace's equation,

$$A_p f_i = B_p f_b \tag{6}$$

Suppose there are N vertices in the tetrahedral mesh M, m of them are interior vertices and n of them are boundary vertices, i.e., vertices on ∂M^+ and ∂M^-. Then A_p is an $m \times m$ matrix, B_p is an $m \times n$ matrix and $L_p = [A_p \ B_p]$; f_i is an $m \times 1$ vector, representing the unknown function values on interior vertices; f_b is an $n \times 1$ vector, representing function values on boundary vertices, whose values are fixed. After solving Eq. 6, the function f acquires a value at each interior vertex. Figure 4b shows a commonly used voxel mesh example (Wüstefeld 2010), where each voxel is a tiny cube. Compared with the voxel mesh, our tetrahedral mesh may have a smoother surface and achieve sub-voxel numerical accuracy.

After solving the Laplace's equation, we build a harmonic field between two surface patches. On the harmonic field, the level sets of equal harmonic function values construct different layers. Figure 4c shows an example of computed surface layers. The different layers, i.e., the equipotential level sets, are labeled with different colors. The left panel shows a volumetric rendering. The right panel shows a zoomed-in result after a cut along the sagittal direction. Similar to prior work (Jones et al. 2000; Adamson et al. 2011), the streamlines are computed by tracing the normal directions to the surface level sets (as shown by the red lines in the zoom-in picture in Fig. 4d). Finally, the computed streamline lengths define the thickness profile on the callosal surface (Jones et al. 2000; Adamson et al. 2011). Figure 4e is the thickness color map on a CC surface, shown in two different views. The red color means thick and the green color means thin. From the figure, we can see that the estimated callosal thickness is well defined. It may reflect the intrinsic 3D geometrical structure and hence facilitate consistent cross-subject comparisons.

Surface Registration

To study CC shape morphometry, surface registration is required to statistically compare CC surfaces from different subjects. A commonly applied framework for surface registration is to map each of the 3D surfaces to a canonical parameter domain, such as a sphere (Bakircioglu et al. 1999; Fischl et al. 1999; Yeo et al. 2010), or a planar domain (Thompson et al. 2004b; Shi et al. 2013a), then compute a flow in the parameter space of two surfaces, which also induces a correspondence field in 3D. In this paper, we apply the conformal parameterization computed with the holomorphic one-form method ("Surface Conformal Parameterization and Decomposition" section) to conformally map the superior and inferior patches of a CC surface to planar rectangles, as shown in Fig. 5a. We use the planar rectangles as the canonical parameter domain for CC surface registration. We then register CC surfaces across subjects using the constrained harmonic map (Wang et al. 2011). Briefly, given two surfaces S_1 and S_2, $\partial S_1, \partial S_2$ are their boundaries, and $\tau_1: S_1 \to \mathbb{R}^2$, $\tau_2: S_2 \to \mathbb{R}^2$ are their conformal parameterizations, our goal is to compute a map $\phi: S_1 \to S_2$. Instead of directly computing ϕ with 3D surfaces, we construct a harmonic map $\tau: \tau_1 \to \tau_2$ between the parameter domains, which satisfies $\tau \circ \tau_1(S_1)=\tau_2(S_2)$, $\tau \circ \tau_1(\partial S_1)=\tau_2(\partial S_2)$, $\Delta\tau=0$. Then ϕ is obtained by $\phi=\tau_2^{-1} \circ \tau \circ \tau_1$. In the registration process, thickness measurement on each surface point is interpolated.

Multivariate Morphometry Features Computation

In addition to CC thickness, we also measure CC surface deformations using surface multivariate tensor-based morphometry analysis (mTBM). After the CC surfaces are registered to a common template, the Jacobian matrix is computed at each vertex from the deformation fields (Wang et al. 2010). Specifically, suppose $\phi: S_1 \to S_2$ is the map between two CC surfaces S_1 and S_2, (u,v) are the isothermal coordinates of the

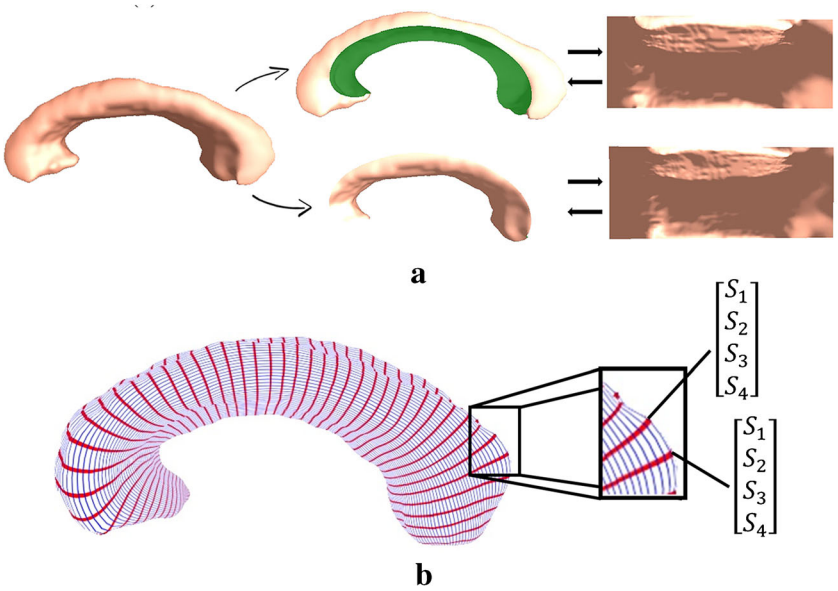

Fig. 5 CC surface registration and multivariate statistics computation. With the conformal parameterization, both the superior and inferior pieces of a CC surface are conformally mapped to a rectangle in the parameter domain (**a**). The shading effect in the parameter space is generated by rendering the surface normal directions of the original 3D surface. We register two CC surfaces in the simpler planar parameter domain, which also induces a registration of the 3D surfaces. The multivariate tensor-based morphometry (mTBM) is then computed on each surface point as a 3×1 vector. The thickness measurement is interpolated on each surface point. The multivariate statistics consisting of the thickness and mTBM are 4×1 vectors on surface vertices (**b**)

surfaces. The map ϕ can be represented as $\phi(u,v)=(\phi_u(u,v), \phi_v(u,v))$ in the local parameters. Then the Jacobian matrix J of ϕ is defined as $J = \begin{bmatrix} \frac{\partial \phi_u}{\partial u} & \frac{\partial \phi_u}{\partial v} \\ \frac{\partial \phi_v}{\partial u} & \frac{\partial \phi_v}{\partial v} \end{bmatrix}$. In practice, smooth surfaces are approximated by triangular meshes. Suppose a triangle $[v_1,v_2,v_3]$ on mesh M_1 is mapped to a triangle $[w_1,w_2,w_3]$ on another mesh M_2. First, we isometrically embed the triangles onto $\mathbb{R}^2$, the planar coordinates of the vertices v_i,w_i are denoted by the same symbols v_i,w_i. Then the Jacobian matrix can be computed as $J=[w_3-w_1,\ w_2-w_1][v_3-v_1,v_2-v_1]^{-1}$. As pointed out in (Leporé et al. 2008), the determinant of the Jacobian matrix is an important measure of local area changes and their directions, i.e., expansion or shrinkage, however, when many subjects are aligned to the same template, much of the shape change information is lost using this measure. Thus we use the deformation tensor for the analysis, which is defined as $S = \left(J^T J\right)^{\frac{1}{2}}$. By definition, the deformation tensor is a 2×2 symmetric matrix with three distinct elements on each vertex. The directional values of shape changes are thus kept as variables in the analysis (Leporé et al. 2008). Furthermore, instead of analyzing shape change directly on the deformation tensor, a new family of metrics, the "Log-Euclidean metrics" (Arsigny et al. 2006) is used in mTBM to project the deformation tensors to a flat space, the tangent plane at the origin of the manifold of deformation tensors (Leporé et al. 2008; Wang et al. 2010). This conversion makes computations on tensors easier to perform, as the transformed values form a vector space, and statistical parameters can then be computed easily using standard formulae for the Euclidean space. In mTBM, this amounts to taking the three distinct elements of $\log(S)$ to form a 3×1 vector, which retains full information of the deformation tensor. Thus, mTBM is very sensitive to deformations such as dilation and shear along the surface tangent direction, which is perpendicular to the surface normal (Wang et al. 2010). On the other hand, the callosal thickness mainly describes morphometric changes along the surface normal direction. Thus, these two statistics are complementary to each other. In this work, we construct a multivariate surface morphometry feature consisting of both callosal thickness and mTBM to boost the detection power (Wang et al. 2011; Shi et al. 2014). Specifically, the multivariate feature is a 4×1 vector on each vertex, as shown in Fig. 5b.

Statistical Maps and Analysis on Group Difference

We aim to study morphological differences in the CC shape between three visual groups. For this analysis, we linearly covary the multivariate statistics at each pixel with subject age and gender information (Leporé et al. 2008; Shi et al. 2013c). Suppose $[A_1,A_2,A_3,A_4]^T$ is the multivariate feature vector on a vertex, let A represent any one of the four statistics, and *Acov*

is the new adjusted statistic. Then *Acov* is computed by fitting the following general linear model to A:

$$A = \beta_0 + \beta_1 \times age + \beta_2 \times gender + \beta_3 \times group + error \quad (7)$$

where β_i, $i=0,1,2,3$ are estimated regression coefficients at the specific vertex. For between-group difference studies, group is coded as a binary dummy variable (e.g., group=0 (SC) and 1 (CB) for SC vs. CB group comparison study) and similarly for gender (i.e., gender =0 (male) and 1 (female)) so that $Acov=\beta_3\times group+error=A-\beta_0-\beta_1\times age-\beta_2\times gender$. For the multivariate measures, the regression is computed separately for each channel (Leporé et al. 2008; Shi et al. 2013c) and on each vertex, we get a new multivariate feature vector $[Acov_1,Acov_2,Acov_3,Acov_4]$.

We apply Hotelling's T^2 test—the multivariate equivalence of the *t*-test—on the multivariate statistics. Given two groups of $n\times 4$ matrices (n is the number of vertices on each surface; and each row is the multivariate feature vector on each vertex), S_i, $i=1,2,\ldots,p$ and T_j, $j=1,2,\ldots q$, we use the Mahalanobis distance M to measure the group mean difference,

$$M = \frac{N_s N_T}{N_s + N_T}\left(\overline{S}-\overline{T}\right)^T \Sigma^{-1}\left(\overline{S}-\overline{T}\right) \quad (8)$$

where N_s and N_T are subject numbers in two groups, $\overline{S}$ and $\overline{T}$ are the means of the two groups and Σ is the combined covariance matrix of two groups (Leporé et al. 2008). In order not to assume normally distributed data, we run a permutation test where we randomly assign subjects to groups. We compare the results (T^2 values) from true labels to the distribution generated from the randomly assigned ones. In each case, the covariate (group membership) was permuted 5000 times and a null distribution was developed for the areas of the average surface with group-difference statistics above the pre-defined threshold in the significance *p* maps. The global map significance is defined as the probability of finding, by chance alone, a statistical map with at least as large a surface area beating the pre-defined statistical threshold of $p=0.05$, under the null hypothesis of no systematic group differences. This omnibus *p*-value is commonly referred to as the *overall significance of the map* (or the features in the map), corrected for multiple comparisons (Wang et al. 2010).

Results

Volumetric Differences Between Groups

We first tested if there were statistical differences in the whole volume of the CCs between any two of three groups (CB, LB and SC). In this experiment, we took the volume of each CC surface as a univariate statistic and applied Student's *t*-test to study group difference. For each pair-wise group comparison, we performed a permutation test with 5000 random assignments of subjects to groups, given 0.05 as the significant level. Total callosal volumes were not significantly different between groups after adjusting for age and gender information (CB vs. SC, $p=0.7774$; CB vs. LB, $p=0.3213$; LB vs. SC, $p=0.3347$).

Linking Callosal Morphometry and Visual Experience

Figure 6 shows statistical maps of callosal morphometry changes in CB vs. SC, CB vs. LB and LB vs. SC. Our method picked up strong differences in CC morphometry for all three group comparisons. In three sets of results, we detected significant areas around splenium areas for the combined measure. The CB also shows significant changes in the body of the CC. After multiple comparisons correction, the overall significances of the multivariate statistics for all three group comparison tests were statistically significant (CB vs. SC, $p=0.0002$; CB vs. LB, $p=0.0123$; LB vs. SC, $p=0.0106$).

Comparison with Other Morphometric Statistics

To explore whether combining thickness with surface area information from mTBM provides additional statistical power, in each experiment, we also conducted three additional statistical tests, including: (1) the thickness (THK) itself; (2) TBM, i.e., the determinant of the Jacobian matrix (Davatzikos 1996; Chung et al. 2008), which gives the magnitude of area changes but not their direction changes; and (3) mTBM alone (Leporé et al. 2008; Wang et al. 2010). For statistics (1) and (2), we applied the Student's *t*-test to compute the group mean difference at each surface point. In case (3) and for our new combined measure, we used Hotelling's T^2 test to compute the group mean difference. Figure 7 shows statistical maps of callosal morphometry changes in CB vs. SC, CB vs. LB and LB vs. SC with these three statistics. The statistical maps of callosal morphometry changes in CB vs. SC, CB vs. LB and LB vs. SC with these three statistics were consistent with the new multivariate statistical maps but with fewer significant areas. We also computed the overall significance of the maps with all three kinds of statistics (as summarized in Table 1). In each of our three group difference analyses, we found that the combined thickness and area multivariate statistics always achieved the most significant values among four statistics.

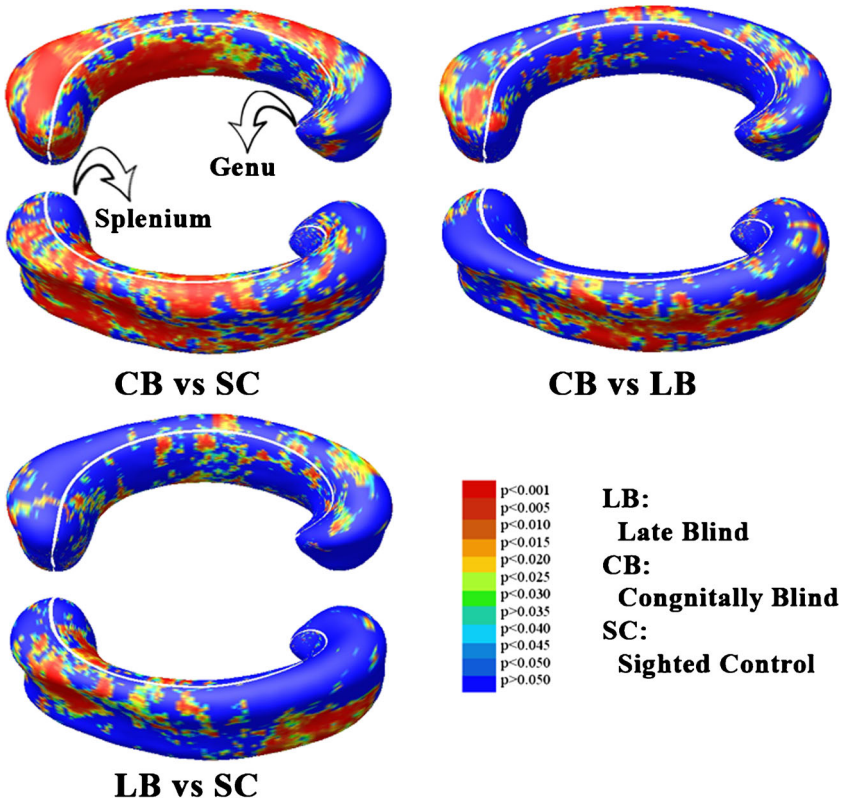

Fig. 6 *P*-maps using the combined mTBM-thickness statistic for the three different group comparisons

The experimental results provide empirical evidence to support the improved statistical power when we combine thickness and mTBM statistics.

Discussion

There are two main contributions in this paper, one methodological and the other theoretical. First, we propose new multivariate statistics by combining the callosal thickness computed from our new method and mTBM. We propose an efficient tetrahedral mesh based method to compute the harmonic field. Our approach adopts a high quality, adaptive tetrahedral mesh (Lederman et al. 2011) and a volumetric Laplace-Beltrami operator (Wang et al. 2004a). Compared with prior work (Jones et al. 2000; Adamson et al. 2011), our partial differential equation (PDE) solving computation may achieve sub-voxel accuracy. Also because surfaces are easily computed from tetrahedral meshes, our method can be easily integrated with prior surface registration work (Wang et al. 2010, 2011, 2013c). Second, we identify areas that show differences in the structure of the CC between early blinds, late blinds and sighted controls. Group difference analysis is an important tool to illustrate the impacts of diseases on brain structures. Specifically, the statistical *p*-maps of group comparisons pinpoint the location and rate of changes and provide a visual index of how a disease affects the shape of brain structures. With permutation test to correct for multiple comparisons, the overall significance *p*-value of a *p*-map is a quantitative measure indicating how likely the patterns in the *p*-map occurring by accident. Group difference analysis has been applied widely in the literature to study the impacts of Alzheimer's disease (AD) on hippocampus and ventricles (Thompson et al. 2004a; Wang et al. 2011), the genetic influence of ApoE4 on hippocampus (Shi et al. 2014), and the impact of prematurity on putamen (Shi et al. 2013b), etc. With group difference analysis, our results confirm and extend prior works by demonstrating how blindness acquired at different periods during development influence the structural reorganization of the CC (e.g., Leporé et al. (2010)).

In contrast to previous structural studies investigating changes in volume of occipital regions and showing massive volume reduction in blind individuals (CB and LB) (Ptito et al. 2008; Qin et al. 2013; Park et al. 2009), we show here that the global volume of the CC remains identical in early and late blind individuals when compared to sighted controls. However, our results highlight that splenium regions, a structure primarily composed of fibers connecting the visual areas of the brain are sensitive to visual deprivation. Our results are consistent with tractographic studies (Shimony et al. 2006; Yu et al. 2007), which found that fractional anisotropy was significantly reduced in the splenium of CB subjects. A voxel-

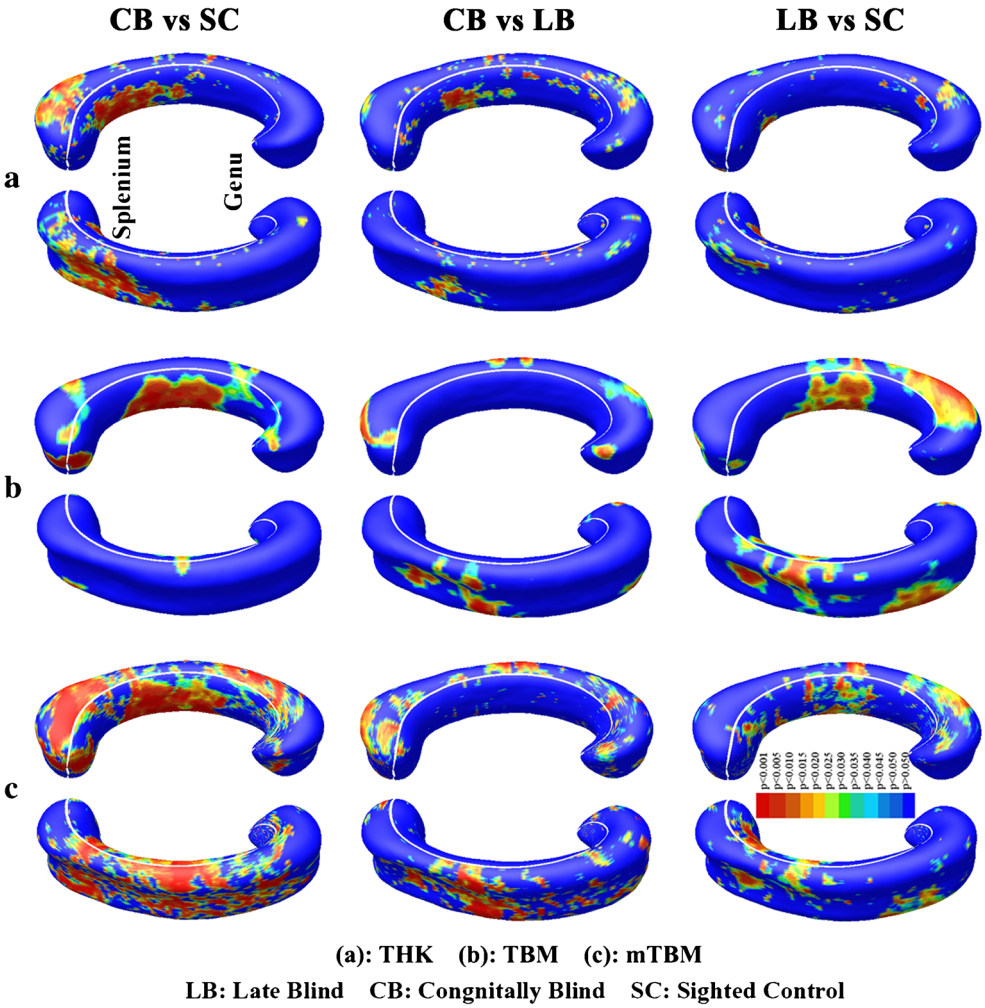

Fig. 7 Comparison of *p*-maps with three statistics for three other different group difference studies. *Non-blue colors* show vertices with statistical differences, at the 0.05 level, uncorrected. The combined multivariate statistics outperforms all three individual statistics (the critical *p*-values for these maps are shown in Table 1)

based morphometric study also reported white matter decreases in the posterior part of the corpus callosum (Ptito et al. 2008). Importantly, we observed that these reorganizations are more significant in individuals deprived of vision early in life compared to blindness acquired late in life. Whereas it has been suggested the existence of a critical period beyond which little or no structural reorganization is possible in the blind (Noppeney 2007; Jiang et al. 2009), we demonstrate here for the first time that visual deprivation acquired after the development of the visual cerebral architecture still impact on the structure of splenial regions of the CC. However, the impact of visual deprivation on the structure of splenial regions is reduced when blindness is acquired late in development. In the late-onset blind subjects, the process of myelination is advanced, so that the structure of the corpus callosum may be more resistant to the change induced by the loss of visual perception.

Our results however contrast with two recent studies that did not observe significant differences in splenial volume and no difference in the gross topographic organization of visual callosal connections in anophthalmic and early blind individuals (Bock et al. 2013; Bridge et al. 2009). Our larger sample size (14 CB were included in our study relative to 6 CB in the Bock's study) may allow greater detection power of volumetric differences within the splenium. More importantly, we introduce here a novel framework to capture a complete set of shape differences in the CC, by combining manual segmentation from T1-weighted brain MRI, modelisation by 3D

Table 1 Permutation-based overall significances of the group difference maps levels, i.e., corrected *p*-values, are shown, after analyzing various different surface-based statistics for pair-wise group comparisons. To detect group differences on CC morphometry, it was advantageous to combine both thickness and full tensor (represented by mTBM) information

	mTBM+Thickness	mTBM	Thickness	TBM
CB vs SC	**0.0002**	0.0052	0.0051	0.0165
CB vs LB	**0.0123**	0.0443	0.1229	0.2052
LB vs SC	**0.0106**	0.0225	0.1776	0.0181

In each of the three group difference analyses, the combined thickness and mTBM multivariate statistics always achieved the most significant values (boldface) among four statistics

tetrahedral meshes and multivariate statistics in order to compare the combination of area and thickness at each point between subject groups. The enhanced sensitivity of this technique is evidenced by the fact that in a previous study, we did not observe any volumetric difference in the CC between LB versus CB or SC groups (Leporé et al. 2010), whereas such differences are compellingly demonstrated here. These results therefore suggest that the newly proposed multivariate morphometry has more detection power in terms of effect size, likely because it captures callosal thickness and more directional and rotational information when measuring geometric differences. Statistically, the improved effect size with the new morphometry is more likely caused by real anatomical differences, instead of bias in the mathematical model or the processing pipeline. When examining the significance of the group differences, we use a non-parametric permutation method in which the subjects are repeatedly assigned into random groups and *p*-values for group differences are computed ("Statistical Maps and Analysis on Group Difference" section). Thus, any bias in the mathematical model should also be found in the permutation distribution that is used to verify the significance of the statistical maps. If there exists bias in the processing pipeline that tends to cause the observations to deviate from their true values in some cases but not in others, then the confound should also present in the situations in which subjects are randomly assigned to groups, and this confound should enter into the permutation distribution, too, protecting against an inflation of Type I error (false positives). It is worth noting here that our observation of between-groups volumetric differences in the splenium part of the CC does not exclude that the retinotopic organization within the splenium itself is not maintained (Bock et al. 2013). Therefore, despite the fact that the large-scale topography of visual callosal tracks may remain intact in blind individuals (Bock et al. 2013), our results suggest that visual deprivation early and even late in life can affect the integrity of these tracks by putatively reducing the myelinisation of these fibers or their axon diameter in the absence of visual input. In addition to provide new insights into the myelinisation and cortical plasticity processes of the CC ensuing visual deprivation, our experiment also opens new avenues for exploring structural differences in various brain regions following visual deprivation.

Our results are also consistent with prior discoveries from animal model studies, e.g., in rats (Olavarria et al. 1987; Chan et al. 2012; Bock and Olavarria 2011), hamsters (Fish et al. 1991), cats (Olavarria and Van Sluyters 1995) and ferrets (Bock et al. 2010, 2012). These studies all demonstrated the significant effects of early enucleation upon brain visual systems. Particularly, it was shown that the pattern of callosal connections was highly anomalous in early enucleated ferrets but that later enucleation had less significant effect on the callosal pattern.

The Corpus callosum is the largest inter-hemispheric commissure in human brain, consisting of over 200 million fibers. Due to the strong contrast with surrounding tissues in MRI scans, it is convenient to apply surface-based algorithms to analyze CC morphometry. However, existing methods on CC study usually delineate the midsagittal section of the CC structure and represent the superior and inferior boundaries as 3D curves. Thickness computed on the curves was used as a measure of local area differences on CC (Thompson et al. 2006; Luders et al. 2010; Joshi et al. 2013). Only a few studies directly worked on CC surfaces (He et al. 2009; Wang et al. 2012b) and used surface areas as potential CC morphometry biomarkers for autism (He et al. 2009) and prematurity (Wang et al. 2012b) research. Our current method may provide a novel way to measure and combine CC thickness and local surface area differences to increase statistical power on CC morphometry study, particularly on blindness research. On the other hand, although the ground truth is not known in defining real biological differences in CC shape between different groups, consistent findings on different datasets with different algorithms may indicate a fair measurement of the efficacy of a novel method. The volume-based study (Leporé et al. 2010) found significant differences in isthmus and splenium of the CB group, which is consistent with our result. Although no significant difference was detected in the LB group, the statistical *p*-map still showed a consistent pattern with our result. A more recent CC study (Tomaiuolo et al. 2014) on a larger dataset (28 CB and 28 SC) also revealed significant regional differences in the splenium, isthmus and the posterior part of the CC body. Thus, our mothed may be effective in detecting real differences between different diagnostic groups.

In T1-weighted MRI, its high contrast difference from surrounding structures make accurate mid-sagittal callosal segmentations straightforward for both manual and automatic methods (Thompson et al. 2003; Styner et al. 2005b; Luders et al. 2006, 2010; Herron et al. 2012). Additionally, its functional differentiation along an elongated sagittal axis has allowed researchers to focus on 2D analyses of the mid-sagittal section. The structural MRI based CC structure has been used to study a variety of human development and diseases including Autism (Vidal et al. 2006; Tepest et al. 2010), Schizophrenia (Joshi et al. 2013; Adamson et al. 2011), Huntington's disease (Di Paola et al. 2012) and others. Starting from our prior work on volumetric Laplace-Beltrami operator and mTBM (Wang et al. 2004a, 2010), here we show that we may integrate two different sets of shape features efficiently for 3D CC structural analysis. Our empirical results on blindness study demonstrated that the combined multivariate statistics improved the statistical power of CC analysis and outperformed some other statistics. Our analysis pipeline is generic and may be applied to analyze CC structures for other neuroinformatics research. We hope our work can provide some practical experience and inspire more interest in combining thickness and surface mTBM features in future CC morphometric study.

Conclusion

We compared the structure of the CC in three groups of subjects with different visual experiences, a congenitally and late blind group and a sighted group. We found significant differences between any two of these three groups, particularly in the splenium part of the CC. These changes were detected using a new MRI-based computer-assisted callosal morphometry system that uses volumetric thickness and surface conformal maps to induce well-organized grids on surfaces. The thickness estimation adopts the tetrahedral mesh based Laplace-Beltrami operator and thus achieves sub-voxel accuracy. The multiple comparisons results demonstrate that our framework may have stronger statistical power than those of thickness or other surface morphometry statistics.

Because of the well-known relationship existing between brain structure and brain function (Zatorre et al. 2012), assessing structural changes in blind individuals may provide important insights onto the functional outcome of sight-restoration (Collignon et al. 2011a), which is timely due to the recent advances in ophthalmologic procedures, stem cell transplantation, genetic therapies, as well as retinal prosthetic devices, which offer now more than ever the hope of restoring sight (Merabet et al. 2005). Such studies may eventually serve to predict outcome in blind individuals who are candidates for sight restoration and pave the way for a new generation of individually-adapted rehabilitation procedures based on the individual neuro-structural profile observed before and after sight restoration (Heimler et al. 2014).

In the future, we will combine and correlate our multivariate statistical framework with other MRI imaging techniques, such as cortical morphometry and diffusion tensor imaging (DTI) tractography, to advance our understanding of how visual deprivation affects the structure of the "visual" brain.

Information Sharing Statement

Data and program source code developed in this manuscript are available under share-alike licenses upon request from N. Leporé and Y. Wang.

Acknowledgments This work was funded by the National Institute on Aging (R21AG043760 to LX, JS and YW), the National Institute for Biomedical Imaging and Bioengineering (R21EB012177 to YL and NL), the Arizona Alzheimer's Consortium (ADHS14-052688 to YW), the National Science Foundation (DMS-1413417, IIS-1421165 to YW), the joint special fund of Shandong province Natural Science Fundation (ZR2013FL008 to GW) and the European Research Council starting grant MADVIS (ERC-StG 337573 to OC). YW is also supported, in part, by U54 EB020403 (the "Big Data to Knowledge" Program), supported by the National Cancer Institute (NCI), the NIBIB and a cross-NIH Consortium.

References

Adamson, C. L., Wood, A. G., Chen, J., Barton, S., Reutens, D. C., Pantelis, C., et al. (2011). Thickness profile generation for the corpus callosum using Laplace's equation. *Human Brain Mapping, 32*(12), 2131–2140. doi:10.1002/hbm.21174.

Amedi, A., Raz, N., Pianka, P., Malach, R., & Zohary, E. (2003). Early 'visual' cortex activation correlates with superior verbal memory performance in the blind. *Nature Neuroscience, 6*(7), 758–766. doi:10.1038/nn1072.

Arsigny, V., Fillard, P., Pennec, X., & Ayache, N. (2006). Log-Euclidean metrics for fast and simple calculus on diffusion tensors. *Magnetic Resonance in Medicine, 56*(2), 411–421.

Bakircioglu, M., Joshi, S., & Miller, M. I. (1999). Landmark matching on brain surfaces via large deformation diffeomorphisms on the sphere. *Proceedings of SPIE Medical Imaging, 3661*, 710–715.

Bavelier, D., & Neville, H. J. (2002). Cross-modal plasticity: where and how? *Nature Reviews Neuroscience, 3*(6), 443–452. doi:10.1038/nrn848.

Bedny, M., Pascual-Leone, A., Dodell-Feder, D., Fedorenko, E., & Saxe, R. (2011). Language processing in the occipital cortex of congenitally blind adults. *Proceedings of the National Academy of Sciences of the United States of America, 108*(11), 4429–4434. doi:10.1073/pnas.1014818108.

Belluck, P. (2013). *Device offers partial vision for the blind*. The New York Times.

Bock, A. S., & Olavarria, J. F. (2011). Neonatal enucleation during a critical period reduces the precision of cortico-cortical projections in visual cortex. *Neuroscience Letters, 501*(3), 152–156. doi:10.1016/j.neulet.2011.07.005.

Bock, A. S., Olavarria, J. F., Leigland, L. A., Taber, E. N., Jespersen, S. N., & Kroenke, C. D. (2010). Diffusion tensor imaging detects early cerebral cortex abnormalities in neuronal architecture induced by bilateral neonatal enucleation: an experimental model in the ferret. *Frontiers in Systems Neuroscience, 4*, 149. doi:10.3389/fnsys.2010.00149.

Bock, A. S., Kroenke, C. D., Taber, E. N., & Olavarria, J. F. (2012). Retinal input influences the size and corticocortical connectivity of visual cortex during postnatal development in the ferret. *Journal of Comparative Neurology, 520*(5), 914–932. doi:10.1002/cne.22738.

Bock, A. S., Saenz, M., Tungaraza, R., Boynton, G. M., Bridge, H., & Fine, I. (2013). Visual callosal topography in the absence of retinal input. *NeuroImage, 81*, 325–334. doi:10.1016/j.neuroimage.2013.05.038.

Bridge, H., Cowey, A., Ragge, N., & Watkins, K. (2009). Imaging studies in congenital anophthalmia reveal preservation of brain architecture in 'visual' cortex. *Brain, 132*(Pt 12), 3467–3480. doi:10.1093/brain/awp279.

Caleo, M., Innocenti, G. M., & Ptito, M. (2013). Physiology and plasticity of interhemispheric connections. *Neural Plasticity, 2013*, 176183. doi:10.1155/2013/176183.

Chan, K. C., Cheng, J. S., Fan, S., Zhou, I. Y., Yang, J., & Wu, E. X. (2012). In vivo evaluation of retinal and callosal projections in early postnatal development and plasticity using manganese-enhanced MRI and diffusion tensor imaging. *NeuroImage, 59*(3), 2274–2283. doi:10.1016/j.neuroimage.2011.09.055.

Chung, M. K. (2012). *Computational neuroanatomy: The methods*. World Scientific Publishing Company.

Chung, M. K., Dalton, K. M., & Davidson, R. J. (2008). Tensor-based cortical surface morphometry via weighted spherical harmonic representation. *IEEE Transactions on Medical Imaging, 27*(8), 1143–1151.

Collignon, O., Voss, P., Lassonde, M., & Lepore, F. (2009). Cross-modal plasticity for the spatial processing of sounds in visually deprived subjects. *Experimental Brain Research, 192*(3), 343–358. doi:10.1007/s00221-008-1553-z.

Collignon, O., Champoux, F., Voss, P., & Lepore, F. (2011a). Sensory rehabilitation in the plastic brain. *Progress in Brain Research, 191*, 211–231. doi:10.1016/B978-0-444-53752-2.00003-5.

Collignon, O., Vandewalle, G., Voss, P., Albouy, G., Charbonneau, G., Lassonde, M., et al. (2011b). Functional specialization for auditory-spatial processing in the occipital cortex of congenitally blind humans. *Proceedings of the National Academy of Sciences of the United States of America, 108*(11), 4435–4440. doi:10.1073/pnas.1013928108.

Collignon, O., Dormal, G., Albouy, G., Vandewalle, G., Voss, P., Phillips, C., et al. (2013a). Impact of blindness onset on the functional organization and the connectivity of the occipital cortex. *Brain, 136*(Pt 9), 2769–2783. doi:10.1093/brain/awt176.

Collignon, O., Dormal, G., & Lepore, F. (2013b). Building the brain in the dark: Functional and specific crossmodal reorganization in the occipital cortex of blind individuals. In M. Jenkin, J. Steeves, & L. Harris (Eds.), *Plasticity in sensory systems*. Cambridge: Cambridge University Press.

Colom, R., Stein, J. L., Rajagopalan, L., Martínez, K., Hermel, D., Wang, Y., et al. (2013). Hippocampal structure and human cognition: key role of spatial processing and evidence supporting the efficiency hypothesis in females. *Intelligence, in press*.

Davatzikos, C. (1996). Spatial normalization of 3D brain images using deformable models. *Journal of Computer Assisted Tomography, 20*(4), 656–665.

Davatzikos, C., Vaillant, M., Resnick, S. M., Prince, J. L., Letovsky, S., & Bryan, R. N. (1996). A computerized approach for morphological analysis of the corpus callosum. *Journal of Computer Assisted Tomography, 20*(1), 88–97.

Di Paola, M., Luders, E., Cherubini, A., Sanchez-Castaneda, C., Thompson, P. M., Toga, A. W., et al. (2012). Multimodal MRI analysis of the corpus callosum reveals white matter differences in presymptomatic and early Huntington's disease. *Cerebral Cortex, 22*(12), 2858–2866. doi:10.1093/cercor/bhr360.

Dormal, G., Lepore, F., & Collignon, O. (2012). Plasticity of the dorsal "spatial" stream in visually deprived individuals. *Neural Plasticity, 2012*, 687659. doi:10.1155/2012/687659.

Dougherty, R. F., Ben-Shachar, M., Bammer, R., Brewer, A. A., & Wandell, B. A. (2005). Functional organization of human occipital-callosal fiber tracts. *Proceedings of the National Academy of Sciences of the United States of America, 102*(20), 7350–7355. doi:10.1073/pnas.0500003102.

Elad, M., Milanfar, P., & Golub, G. H. (2004). Shape from moments - an estimation theory perspective. *Transactions on Signal Processing, 52*(7), 1814–1829. doi:10.1109/tsp.2004.828919.

Fischl, B., Sereno, M. I., & Dale, A. M. (1999). Cortical surface-based analysis II: inflation, flattening, and a surface-based coordinate system. *NeuroImage, 9*(2), 195–207.

Fish, S. E., Rhoades, R. W., Bennett-Clarke, C. A., Figley, B., & Mooney, R. D. (1991). Organization, development and enucleation-induced alterations in the visual callosal projection of the hamster: single axon tracing with phaseolus vulgaris leucoagglutinin and Di-I. *European Journal of Neuroscience, 3*(12), 1255–1270.

Gu, X., Wang, Y., Chan, T. F., Thompson, P. M., & Yau, S.-T. (2004). Genus zero surface conformal mapping and its application to brain surface mapping. *IEEE Transactions on Medical Imaging, 23*(8), 949–958.

He, Q., Duan, Y., Yin, X., Gu, X., Karsch, K., & Miles, J. (2009) Shape analysis of corpus callosum in autism subtype using planar conformal mapping. *SPIE, Medical Imaging,* 7262. doi:10.1117/12.812285.

Heimler, B., Weisz, N., Collignon, O. (2014) Revisiting the adaptive and maladaptive effects of crossmodal plasticity. *Neuroscience, 283*, 44–63.

Herron, T. J., Kang, X., & Woods, D. L. (2012). Automated measurement of the human corpus callosum using MRI. *Frontiers in Neuroinformatics, 6*, 25. doi:10.3389/fninf.2012.00025.

Hofer, S., & Frahm, J. (2006). Topography of the human corpus callosum revisited–comprehensive fiber tractography using diffusion tensor magnetic resonance imaging. *NeuroImage, 32*(3), 989–994. doi:10.1016/j.neuroimage.2006.05.044.

Hua, X., Leow, A. D., Levitt, J. G., Caplan, R., Thompson, P. M., & Toga, A. W. (2009). Detecting brain growth patterns in normal children using tensor-based morphometry. *Human Brain Mapping, 30*(1), 209–219. doi:10.1002/hbm.20498.

Jenkinson, M., & Smith, S. (2001). A global optimisation method for robust affine registration of brain images. *Medical Image Analysis, 5*(2), 143–156.

Jiang, J., Zhu, W., Shi, F., Liu, Y., Li, J., Qin, W., et al. (2009). Thick visual cortex in the early blind. *Journal of Neuroscience, 29*(7), 2205–2211. doi:10.1523/JNEUROSCI. 5451-08.2009.

Jones, S. E., Buchbinder, B. R., & Aharon, I. (2000). Three-dimensional mapping of cortical thickness using Laplace's equation. *Human Brain Mapping, 11*(1), 12–32.

Joshi, S. H., Narr, K. L., Philips, O. R., Nuechterlein, K. H., Asarnow, R. F., Toga, A. W., et al. (2013). Statistical shape analysis of the corpus callosum in Schizophrenia. *NeuroImage, 64*, 547–559. doi:10.1016/j.neuroimage.2012.09.024.

Lederman, C., Joshi, A., Dinov, I., Vese, L., Toga, A., & Van Horn, J. D. (2011). The generation of tetrahedral mesh models for neuroanatomical MRI. *NeuroImage, 55*(1), 153–164. doi:10.1016/j.neuroimage.2010.11.013.

Leporé, N., Brun, C., Chou, Y.-Y., Chiang, M.-C., Dutton, R. A., Hayashi, K. M., et al. (2008). Generalized tensor-based morphometry of HIV/AIDS using multivariate statistics on deformation tensors. *IEEE Transactions on Medical Imaging, 27*(1), 129–141.

Leporé, N., Shi, Y., Lepore, F., Fortin, M., Voss, P., Chou, Y. Y., et al. (2009). Pattern of hippocampal shape and volume differences in blind subjects. *NeuroImage, 46*(4), 949–957. doi:10.1016/j.neuroimage.2009.01.071.

Leporé, N., Voss, P., Lepore, F., Chou, Y. Y., Fortin, M., Gougoux, F., et al. (2010). Brain structure changes visualized in early- and late-onset blind subjects. *NeuroImage, 49*(1), 134–140. doi:10.1016/j.neuroimage.2009.07.048.

Levin, N., Dumoulin, S. O., Winawer, J., Dougherty, R. F., & Wandell, B. A. (2010). Cortical maps and white matter tracts following long period of visual deprivation and retinal image restoration. *Neuron, 65*(1), 21–31. doi:10.1016/j.neuron.2009.12.006.

Li, X., Guo, X., Wang, H., He, Y., Gu, X., & Qin, H. (2007). *Harmonic volumetric mapping for solid modeling applications.* Paper presented at the Proceedings of the 2007 ACM symposium on Solid and physical modeling, Beijing, China.

Li, B., Li, X., Wang, K., & Qin, H. (2013). Surface mesh to volumetric spline conversion with generalized polycubes. *IEEE Transactions on Visualization and Computer Graphics, 19*(9), 1539–1551. doi:10.1109/tvcg.2012.177.

Lombaert, H., Grady, L., Polimeni, J. R., & Cheriet, F. (2013). FOCUSR: feature oriented correspondence using spectral regularization - a method for accurate surface matching. *IEEE Transactions on Pattern Analysis and Machine Intelligence, 35*(9), 2143–2160.

Luders, E., Narr, K. L., Zaidel, E., Thompson, P. M., Jancke, L., & Toga, A. W. (2006). Parasagittal asymmetries of the corpus callosum. *Cerebral Cortex, 16*(3), 346–354. doi:10.1093/cercor/bhi112.

Luders, E., Thompson, P. M., & Toga, A. W. (2010). The development of the corpus callosum in the healthy human brain. *Journal of Neuroscience, 30*(33), 10985–10990. doi:10.1523/JNEUROSCI.5122-09.2010.

Merabet, L. B., Rizzo, J. F., Amedi, A., Somers, D. C., & Pascual-Leone, A. (2005). What blindness can tell us about seeing again: merging

neuroplasticity and neuroprostheses. *Nature Reviews Neuroscience, 6*(1), 71–77. doi:10.1038/nrn1586.

Merabet, L. B., Rizzo, J. F., 3rd, Pascual-Leone, A., & Fernandez, E. (2007). 'Who is the ideal candidate?': decisions and issues relating to visual neuroprosthesis development, patient testing and neuroplasticity. *Journal of Neural Engineering, 4*(1), S130–S135. doi:10.1088/1741-2560/4/1/S15.

Monje, M., Thomason, M. E., Rigolo, L., Wang, Y., Waber, D. P., Sallan, S. E., et al. (2013). Functional and structural differences in the hippocampus associated with memory deficits in adult survivors of acute lymphoblastic leukemia. *Pediatric Blood & Cancer, 60*(2), 293–300. doi:10.1002/pbc.24263.

Noppeney, U. (2007). The effects of visual deprivation on functional and structural organization of the human brain. *Neuroscience and Biobehavioral Reviews, 31*(8), 1169–1180. doi:10.1016/j.neubiorev.2007.04.012.

Noppeney, U., Friston, K. J., Ashburner, J., Frackowiak, R., & Price, C. J. (2005). Early visual deprivation induces structural plasticity in gray and white matter. *Current Biology, 15*(13), R488–R490. doi:10.1016/j.cub.2005.06.053.

Olavarria, J. F., & Van Sluyters, R. C. (1995). Overall pattern of callosal connections in visual cortex of normal and enucleated cats. *Journal of Comparative Neurology, 363*(2), 161–176. doi:10.1002/cne.903630202.

Olavarria, J., Malach, R., & Van Sluyters, R. C. (1987). Development of visual callosal connections in neonatally enucleated rats. *Journal of Comparative Neurology, 260*(3), 321–348. doi:10.1002/cne.902600302.

Pai, D., Soltanian-Zadeh, H., & Hua, J. (2011). Evaluation of fiber bundles across subjects through brain mapping and registration of diffusion tensor data. *NeuroImage, 54*(Suppl 1), S165–S175. doi:10.1016/j.neuroimage.2010.05.085.

Paillé, G.-P., & Poulin, P. (2012). SMI 2012: full as-conformal-as-possible discrete volumetric mapping. *Computers and Graphics, 36*(5), 427–433. doi:10.1016/j.cag.2012.03.014.

Pan, W. J., Wu, G., Li, C. X., Lin, F., Sun, J., & Lei, H. (2007). Progressive atrophy in the optic pathway and visual cortex of early blind Chinese adults: a voxel-based morphometry magnetic resonance imaging study. *NeuroImage, 37*(1), 212–220. doi:10.1016/j.neuroimage.2007.05.014.

Pandya, D. N., Karol, E. A., & Heilbronn, D. (1971). The topographical distribution of interhemispheric projections in the corpus callosum of the rhesus monkey. *Brain Research, 32*(1), 31–43.

Park, H. J., Jeong, S. O., Kim, E. Y., Kim, J. I., Park, H., Oh, M. K., et al. (2007). Reorganization of neural circuits in the blind on diffusion direction analysis. *Neuroreport, 18*(17), 1757–1760. doi:10.1097/WNR.0b013e3282f13e66.

Park, H. J., Lee, J. D., Kim, E. Y., Park, B., Oh, M. K., Lee, S., et al. (2009). Morphological alterations in the congenital blind based on the analysis of cortical thickness and surface area. *NeuroImage, 47*(1), 98–106. doi:10.1016/j.neuroimage.2009.03.076.

Ptito, M., Schneider, F. C., Paulson, O. B., & Kupers, R. (2008). Alterations of the visual pathways in congenital blindness. *Experimental Brain Research, 187*(1), 41–49. doi:10.1007/s00221-008-1273-4.

Qin, W., Liu, Y., Jiang, T., & Yu, C. (2013). The development of visual areas depends differently on visual experience. *PloS One, 8*(1), e53784. doi:10.1371/journal.pone.0053784.

Qiu, A., Bitouk, D., & Miller, M. I. (2006a). Smooth functional and structural maps on the neocortex via orthonormal bases of the Laplace-Beltrami operator. *IEEE Transactions on Medical Imaging, 25*(10), 1296–1306.

Qiu, A., Rosenau, B. J., Greenberg, A. S., Hurdal, M. K., Barta, P., Yantis, S., et al. (2006b). Estimating linear cortical magnification in human primary visual cortex via dynamic programming. *NeuroImage, 31*(1), 125–138. doi:10.1016/j.neuroimage.2005.11.049.

Ricciardi, E., & Pietrini, P. (2011). New light from the dark: what blindness can teach us about brain function. *Current Opinion in Neurology, 24*(4), 357–363. doi:10.1097/WCO.0b013e328348bdbf.

Shi, Y., Lai, R., Morra, J. H., Dinov, I., Thompson, P. M., & Toga, A. W. (2010). Robust surface reconstruction via Laplace-Beltrami eigen-projection and boundary deformation. *IEEE Transactions on Medical Imaging, 29*(12), 2009–2022. doi:10.1109/TMI.2010.2057441.

Shi, J., Thompson, P. M., Gutman, B., & Wang, Y. (2013a). Surface fluid registration of conformal representation: application to detect disease burden and genetic influence on hippocampus. *NeuroImage, 78C*, 111–134. doi:10.1016/j.neuroimage.2013.04.018.

Shi, J., Wang, Y., Ceschin, R., An, X., Lao, Y., Vanderbilt, D., et al. (2013b). A multivariate surface-based analysis of the putamen in premature newborns: regional differences within the ventral striatum. *PloS One, 8*(7), e66736. doi:10.1371/journal.pone.0066736.

Shi, R., Zeng, W., Su, Z., Damasio, H., Lu, Z., Wang, Y., et al. (2013c, June) Hyperbolic Harmonic Mapping for Constrained Brain Registration. In *IEEE Conf. Comp. Vis. Patt. Recog. CVPR'13*.

Shi, J., Lepore, N., Gutman, B. A., Thompson, P. M., Baxter, L. C., Caselli, R. L., et al. (2014). Genetic influence of apolipoprotein E4 genotype on hippocampal morphometry: an N=725 surface-based Alzheimer's disease neuroimaging initiative study. *Human Brain Mapping*. doi:10.1002/hbm.22447.

Shimony, J. S., Burton, H., Epstein, A. A., McLaren, D. G., Sun, S. W., & Snyder, A. Z. (2006). Diffusion tensor imaging reveals white matter reorganization in early blind humans. *Cerebral Cortex, 16*(11), 1653–1661. doi:10.1093/cercor/bhj102.

Shu, N., Li, J., Li, K., Yu, C., & Jiang, T. (2009). Abnormal diffusion of cerebral white matter in early blindness. *Human Brain Mapping, 30*(1), 220–227. doi:10.1002/hbm.20507.

Sieving, P. A., Caruso, R. C., Tao, W., Coleman, H. R., Thompson, D. J. S., Fullmer, K. R., et al. (2006). Ciliary neurotrophic factor (CNTF) for human retinal degeneration: phase I trial of CNTF delivered by encapsulated cell intraocular implants. *Proceedings of the National Academy of Sciences of the United States of America, 103*(10), 3896–3901. doi:10.1073/pnas.0600236103.

Steele, C. J., Bailey, J. A., Zatorre, R. J., & Penhune, V. B. (2013). Early musical training and white-matter plasticity in the corpus callosum: evidence for a sensitive period. *Journal of Neuroscience, 33*(3), 1282–1290. doi:10.1523/JNEUROSCI. 3578-12.2013.

Styner, M., Lieberman, J. A., McClure, R. K., Weinberger, D. R., Jones, D. W., & Gerig, G. (2005a). Morphometric analysis of lateral ventricles in schizophrenia and healthy controls regarding genetic and disease-specific factors. *Proceedings of the National Academy of Sciences of the United States of America, 102*(13), 4872–4877.

Styner, M. A., Oguz, I., Smith, R. G., Cascio, C., & Jomier, M. (2005b). Corpus callosum subdivision based on a probabilistic model of inter-hemispheric connectivity. *Medical Image Computing and Computer-Assisted Intervention, 8*(Pt 2), 765–772.

Tan, Y., Hua, J., & Qin, H. (2010). Physically based modeling and simulation with dynamic spherical volumetric simplex splines. *Computer-Aided Design, 42*(2), 95–108. doi:10.1016/j.cad.2009.02.014.

Tepest, R., Jacobi, E., Gawronski, A., Krug, B., Moller-Hartmann, W., Lehnhardt, F. G., et al. (2010). Corpus callosum size in adults with high-functioning autism and the relevance of gender. *Psychiatry Research, 183*(1), 38–43. doi:10.1016/j.pscychresns.2010.04.007.

Thompson, P. M., Giedd, J. N., Woods, R. P., MacDonald, D., Evans, A. C., & Toga, A. W. (2000). Growth patterns in the developing human brain detected using continuum-mechanical tensor mapping. *Nature, 404*(6774), 190–193.

Thompson, P. M., Narr, K. L., Blanton, R. E., & Toga, A. W. (2003). Mapping structural alterations of the corpus callosum during brain development and degeneration. In E. Zaidel & M. Iacobini (Eds.), *The parallel brain: The cognitive neuroscience of the corpus callosum* (pp. 93–130). Cambridge: The MIT Press.

Thompson, P. M., Hayashi, K. M., de Zubicaray, G. I., Janke, A. L., Rose, S. E., Semple, J., et al. (2004a). Mapping hippocampal and ventricular change in Alzheimer's disease. *NeuroImage, 22*(4), 1754–1766.

Thompson, P. M., Hayashi, K. M., Sowell, E. R., Gogtay, N., Giedd, J. N., Rapoport, J. L., et al. (2004b). Mapping cortical change in Alzheimer's disease, brain development, and schizophrenia. *NeuroImage, 23*(Supplement 1), S2–S18.

Thompson, P. M., Dutton, R. A., Hayashi, K. M., Lu, A., Lee, S. E., Lee, J. Y., et al. (2006). 3D mapping of ventricular and corpus callosum abnormalities in HIV/AIDS. *NeuroImage, 31*(1), 12–23. doi:10.1016/j.neuroimage.2005.11.043.

Tomaiuolo, F., Campana, S., Collins, D. L., Fonov, V. S., Ricciardi, E., Sartori, G., et al. (2014). Morphometric changes of the corpus callosum in congenital blindness. *PloS One, 9*(9), e107871. doi:10.1371/journal.pone.0107871.

Veraart, C., Duret, F., Brelen, M., Oozeer, M., & Delbeke, J. (2004). Vision rehabilitation in the case of blindness. *Expert Review of Medical Devices, 1*(1), 139–153. doi:10.1586/17434440.1.1.139.

Vidal, C. N., Nicolson, R., DeVito, T. J., Hayashi, K. M., Geaga, J. A., Drost, D. J., et al. (2006). Mapping corpus callosum deficits in autism: an index of aberrant cortical connectivity. *Biological Psychiatry, 60*(3), 218–225. doi:10.1016/j.biopsych.2005.11.011.

Voss, P., & Zatorre, R. J. (2012). Occipital cortical thickness predicts performance on pitch and musical tasks in blind individuals. *Cerebral Cortex, 22*(11), 2455–2465. doi:10.1093/cercor/bhr311.

Voss, P., Fortin, M., Corbo, V., Pruessner, J. C., & Lepore, F. (2013). Assessment of the caudate nucleus and its relation to route learning in both congenital and late blind individuals. *BMC Neuroscience, 14*, 113. doi:10.1186/1471-2202-14-113.

Wang, Y., Gu, X., Chan, T. F., Thompson, P. M., & Yau, S.-T. (2004a). *Volumetric harmonic brain mapping*. Paper presented at the Biomedical Imaging: Nano to Macro, 2004. IEEE International Symposium on.

Wang, Y., Gu, X., & Yau, S.-T. (2004b). Volumetric harmonic map. *Communications in Information and Systems, 3*(3), 191–202.

Wang, Y., Zhang, J., Gutman, B., Chan, T. F., Becker, J. T., Aizenstein, H. J., et al. (2010). Multivariate tensor-based morphometry on surfaces: application to mapping ventricular abnormalities in HIV/AIDS. *NeuroImage, 49*(3), 2141–2157. doi:10.1016/j.neuroimage.2009.10.086.

Wang, Y., Song, Y., Rajagopalan, P., An, T., Liu, K., Chou, Y. Y., et al. (2011). Surface-based TBM boosts power to detect disease effects on the brain: an N=804 ADNI study. *NeuroImage, 56*(4), 1993–2010. doi:10.1016/j.neuroimage.2011.03.040.

Wang, K., Li, X., Li, B., Xu, H., & Qin, H. (2012a). Restricted trivariate polycube splines for volumetric data modeling. *IEEE Transactions on Visualization and Computer Graphics, 18*(5), 703–716. doi:10.1109/TVCG.2011.102.

Wang, Y., Panigrahy, A., Shi, J., Ceschin, R., Nie, Z., Nelson, M. D., et al. (2012b) 3D vs. 2D surface shape analysis of the corpus collosum in premature neonates. In *MICCAI: Workshop on Paediatric and Perinatal Imaging, Nice, France*.

Wang, Y., Shi, J., Yin, X., Gu, X., Chan, T. F., Yau, S.-T., et al. (2012c). Brain surface conformal parameterization with the Ricci flow. *IEEE Transactions on Medical Imaging, 31*(2), 251–264.

Wang, D., Qin, W., Liu, Y., Zhang, Y., Jiang, T., & Yu, C. (2013a). Altered white matter integrity in the congenital and late blind people. *Neural Plasticity, 2013*, 128236. doi:10.1155/2013/128236.

Wang, G., Li, J., Chen, J., Wang, L., Jiang, Z., Su, Q., et al. (2013b). A heat kernel based brain grey matter morphometry system. Paper presented at the 3rd MICCAI Workshop on Multimodal Brain Image Analysis (MBIA).

Wang, Y., Yuan, L., Shi, J., Greve, A., Ye, J., Toga, A. W., et al. (2013c). Applying tensor-based morphometry to parametric surfaces can improve MRI-based disease diagnosis. *NeuroImage, 74*, 209–230. doi:10.1016/j.neuroimage.2013.02.011.

Wüstefeld, T. (2010). bilderzucht - blog. http://www.bilderzucht.de/blog/3d-pixel-voxel.

Xu, L. (2013). *Combining thickness information with surface tensor-based morphometry for the 3D statistical analysis of the corpus callosum*. Master Thesis, Arizona State University, Tempte, AZ.

Xu, H., Yu, W., Gu, S., & Li, X. (2013a). Biharmonic volumetric mapping using fundamental solutions. *IEEE Transactions on Visualization and Computer Graphics, 19*(5), 787–798. doi:10.1109/TVCG.2012.173.

Xu, L., Collignon, O., Wang, G., Kang, Y., Leporé, F., Shi, J., et al. (2013b). Combining Thickness Information with Surface Tensor-based Morphometry for the 3D Statistical Analysis of the Corpus Callosum. Paper presented at the 4th MICCAI Workshop on Mathematical Foundations of Computational Anatomy (MFCA).

Yeo, B. T., Sabuncu, M. R., Vercauteren, T., Ayache, N., Fischl, B., & Golland, P. (2010). Spherical demons: fast diffeomorphic landmark-free surface registration. *IEEE Transactions on Medical Imaging, 29*(3), 650–668. doi:10.1109/TMI.2009.2030797.

Yu, C., Shu, N., Li, J., Qin, W., Jiang, T., & Li, K. (2007). Plasticity of the corticospinal tract in early blindness revealed by quantitative analysis of fractional anisotropy based on diffusion tensor tractography. *NeuroImage, 36*(2), 411–417. doi:10.1016/j.neuroimage.2007.03.003.

Yushkevich, P. A., Piven, J., Hazlett, H. C., Smith, R. G., Ho, S., Gee, J. C., et al. (2006). User-guided 3D active contour segmentation of anatomical structures: significantly improved efficiency and reliability. *NeuroImage, 31*(3), 1116–1128. doi:10.1016/j.neuroimage.2006.01.015.

Zatorre, R. J., Fields, R. D., & Johansen-Berg, H. (2012). Plasticity in gray and white: neuroimaging changes in brain structure during learning. *Nature Neuroscience, 15*(4), 528–536. doi:10.1038/nn.3045.